Observation of graphene grain boundaries through selective adsorption of rhodamine B using fluorescence microscopy

Dong-Wook Shin [a], Dongchul Sung [e], Ji Su Hong [b], Minwoo Kim [a], Seung Soo Yoon [c], Young-Jae Song [a, d], Gunn Kim [e], Suklyun Hong [e, **], Ji-Beom Yoo [a, b, *]

[a] SKKU Advanced Institute of Nanotechnology (SAINT), Center for Human Interface Nano Technology (HINT), Sungkyunkwan University (SKKU), Suwon, 440-746, Republic of Korea
[b] School of Advanced Materials Science and Engineering (BK21), Sungkyunkwan University (SKKU), Suwon, 440-746, Republic of Korea
[c] Department of Chemistry, Sungkyunkwan University (SKKU), Suwon, 440-746, Republic of Korea
[d] Department of Physics, Sungkyunkwan University (SKKU), Suwon, 440-746, Republic of Korea
[e] Graphene Research Institute and Department of Physics, Sejong University, Seoul, 143-747, Republic of Korea

ARTICLE INFO

ABSTRACT

The graphene grain boundary (GGB), line defect, has a marked influence on an electrical properties and mechanical strength of graphene. Observation of the grain size and defect distribution is important for tuning the properties of graphene. Here we show imaging GGBs with rhodamine B (RB) by fluorescence microscopy (FM), and demonstrate the selective adsorption of RB molecules on the GGBs after a pre-annealing process and RB treatment. The hill structure of oxidized Cu below GGB is formed by a pre-annealing process, and induces RB molecules to selectively physisorb on GGBs due to the interplay between graphene and oxidized Cu, which is directly confirmed by kelvin probe force microscopy (KPFM) and density function theory (DFT) calculation. The selectively adsorbed RB was completely removed by acetone rinsing without disrupting the graphene sheets. This simple observation method provides an efficient and convenient means of evaluating the quality and reliability of graphene as well as other two-dimensional materials, such as WS_2, WSe_2, MoS_2, $MoSe_2$ and BN.

1. Introduction

Chemical vapor deposition (CVD) process for a growth of large-scale and high quality graphene has been investigated extensively for high-volume manufacturing of touch screens, smart windows etc. There are, however, deficiencies in CVD graphene, such as multi-grain boundaries (line defect) and vacancies (point defect), which reduce its intrinsic properties and hinder high-volume manufacturing. Among these, graphene grain boundaries (GGBs), a type of line defect, are composed of graphene domains of various crystalline orientations, formed during the nucleation and initial growth stage. Properties of polycrystalline graphene are dominated by the size of the domains and the atomic rearrangement in grain boundaries, which govern transport properties and related device performance [1,2]. For tailoring intrinsic graphene properties, therefore, observing the GGBs in polycrystalline graphene using a specific tool is significantly important. Generally, GGBs are observed by transmission electron microscopy (TEM) [3,4] and scanning tunneling microscopy (STM) [2,5–9]. To obtain information regarding the distribution of GGBs on a large scale, methods of selectively oxidizing the underlying copper foil of GGBs [10–12] and coating the graphene with liquid crystal [13,14] have been suggested.

Using TEM or STM, the atomic structure and size of GGBs can be clearly observed. These measurements in ultra-high vacuum, however, involve costly and time-consuming sample preparation and measurement processes, and their use for macroscopic assessment of device performance is problematic. To observe the distribution of GGBs over a large area, an easy method using optical microscopy was suggested. Optical birefringence from the transferred graphene covered with a liquid crystal has been used to visualize GGBs, but it is not easy to distinguish the adjacent liquid crystals deposited on the graphene with a small domain size and

misorientation [13,14]. In the method involving oxidizing the underlying copper foil of GGBs [10–12], although the graphene domain size was measured by the oxidation of the graphene/Cu layer, the graphene was exposed to a high temperature of >200 °C in an oxygen environment [11], high humidity [10], and electrolyte [12], resulting in degradation of graphene. Here, we present a new method of observing GGBs using fluorescence molecules and fluorescence microscopy (FM). Rhodamine B (RB) selectively adsorbed on GGBs is readily visualized by FM, and then can be completely removed by immersion in acetone without degrading the graphene. The surface potential of the graphene was changed due to the formation of oxidized Cu below GGBs by pre-annealing in an oxygen environment at 110 °C. Positively charged graphene produced by electron depletion of graphene by the oxidized Cu is induced to selectively adsorb RB molecules on GGBs. Our observations are not limited to graphene; they can be applied to other two-dimensional (2D) materials, such as boron nitride (BN), MoS_2, $MoSe_2$, WSe_2, and WS_2.

2. Experimental

2.1. Graphene growth and attachment of rhodamine B (RB) molecules on GGB

Graphene was synthesized on Cu foil (Wacopa Inc.) by chemical vapor deposition (CVD). Rolled copper foil was inserted into a quartz tube and heated to 1000 °C (heating rate: 17 °C/min) with a flow of 10 sccm of H_2. The copper foils were heat-treated for 30 min to increase the grain size. For the synthesis of graphene, a gas mixture of CH_4 and H_2 was then flowed for 30 min (1000 °C) at rates of 20 and 10 sccm, respectively. Finally, the sample was cooled to 100 °C (10 °C/min) under H_2 flow. Graphene synthesized on Cu foil was annealed under oxygen (O_2 flow, 150 sccm) at 110 °C for 2 h, which is mild oxidation (MO). After MO, cracks (Fig. 1c) on a rolled and distorted Cu foil on which graphene was synthesized during sample preparation process were observed by optical microscopy [10]. RB (Sigma Aldrich) solution (10^{-4} M) in ethanol was prepared in which mildly oxidized graphene/Cu foil was immersed for 20 min.

2.2. Characterization of RB on graphene

The RB treatment of oxidized Cu beneath the GGBs was characterized by fluorescence microscopy (Olympus corp., BX51M, green excitation filter (U-MWGS3), 100 W halogen lamp (U-LH100L-3)), Raman (Witec, 532 nm laser excitation), AFM, and KPFM to visualize RB molecules. In KPFM and AFM, typical tapping mode AFM (NTEGRA SPECTRA AFM-RAMAN from NT-MDT) and the two-path technique were applied to separate the topography effect. Topography was measured first and the tip was raised up 50 nm following the path of the recorded topography. AC modulation of 2–4 V was applied near the resonance frequency of the Pt−Ir−coated tip (PPP-EFM tip, resonance frequency: 45–115 kHz, force constant: 0.5–9.5 N/m; NANOSENSORS). Topography and surface potential images were obtained using a 1 Hz of scan rate.

2.3. Computational methods

To assess the binding behavior of RB on graphene/Cu(111) and graphene/oxidized-Cu(111) substrates, we performed density functional theory (DFT) calculations within generalized gradient approximation (GGA) using the Vienna ad initio simulation package (VASP) [15–18]. Cu(111) substrate, which had the lowest surface energy, was selected instead of polycrystalline Cu (Cu foil) [19]. The projector augmented wave (PAW) potentials, as implemented in

the VASP, were employed to describe the potentials from atom centers. The energy cutoff for the plane-wave basis was set to 400 eV. Geometries were optimized until the Hellman-Feynman forces acting on the atoms became smaller than 0.03 eV/Å. To include weak van der Waals (vdW) interactions among them, we adopted the Grimme's DFT-D3 vdW correction based on a semi-empirical GGA-type theory [20]. For the Brillouin-zone interaction we used $1 \times 1 \times 1$ grid in the Monkhorsk-Pack special k-point scheme.

3. Results and discussion

A fluorescence microscope is generally used to observe bio-materials treated with fluorescence materials (or dyes). Selective reactions between the dyes and biomaterials can be used to observe specific elements in biomaterials by fluorescence microscopy (FM) [21]. In this respect, we used rhodamine B (RB) and FM to image the graphene grain boundaries (GGBs). The selective reaction between GGBs and RB molecules was facilitated by pre-annealing of graphene/Cu foil, followed by RB treatment; RB-treated GGBs were observed by FM. The detailed processes are as follows: (i) A graphene/Cu foil was pre-annealed in an oxygen environment at 110 °C for 2 h to promote mild oxidation of Cu beneath the GGB. (ii) The pre-annealed graphene/Cu foil was dipped in RB solution for 20 min, and then characterized by FM (Fig. 1a). To confirm the selective adsorption of RB on GGBs, RB-treated pristine graphene/Cu foil without pre-annealing was also prepared. Fig. 1c and d show optical and fluorescence images of the RB-treated graphene after pre-annealing, respectively. In the optical image, only a crack in graphene and unevenness (hole) of the Cu foil were observed. The cracks were formed by fracture of graphene due to bending or flattening of the graphene/Cu foil during sample preparation [10]. In contrast to the optical image, GGBs with fluorescence lines of RB as well as a crack and unevenness (hole) were evident by FM (Fig. 1d). From the FM image, 5.68 μm^2 of graphene grain size was obtained. As the temperature of annealing and growth was increased to 1050 °C, the graphene grain size was increased from 5.68 to 9.19 μm^2 (Supplementary Information Fig. S1). In the fluorescence image of RB-treated pristine graphene, the fluorescence line of grain boundaries and unevenness (hole) of Cu without GGBs were apparent (Fig. 1b). The selective adsorption of RB on the GGBs after pre-annealing was confirmed (Fig. 1b and d).

The morphology of RB molecules selectively adsorbed on the GGB was investigated by AFM (Fig. 2a), which showed good agreement with the fluorescence image. The dot-shaped RB molecules were selectively adsorbed on the surface of graphene/Cu (Fig. 2a and e, Supplementary Information Fig. S2). An interesting and unique feature of this new protocol is removal of the RB molecules by dipping in acetone, as shown in Fig. 2b. After removal of RB molecules, although the oxidized Cu was not observed by optical microscopy, as in the optical image of RB-treated graphene (Fig. 1c), hill structures of oxidized Cu were confirmed by AFM (Fig. 2b). Removal of RB molecules from GGB by dipping in acetone was also apparent in the fluorescence image (Fig. 2c). By comparing the surface morphology by AFM before and after RB cleaning, we determined the height of RB molecules and oxidized Cu, respectively, (Fig. 2d). The average height of RB adsorbed GGB on oxidized Cu was 12.17 nm (RB + oxidized Cu), and after RB cleaning their height was 3.88 nm (oxidized Cu, inset to Fig. 2d). The thickness of adsorbed RB molecules, therefore, was estimated to be ~8.29 nm.

Selective adsorption and thickness of RB molecules on GGBs were confirmed by the fluorescence and AFM images of graphene after pre-annealing and RB treatment, whereas their adsorption mechanism is unclear. Previous reports suggested a mechanism for
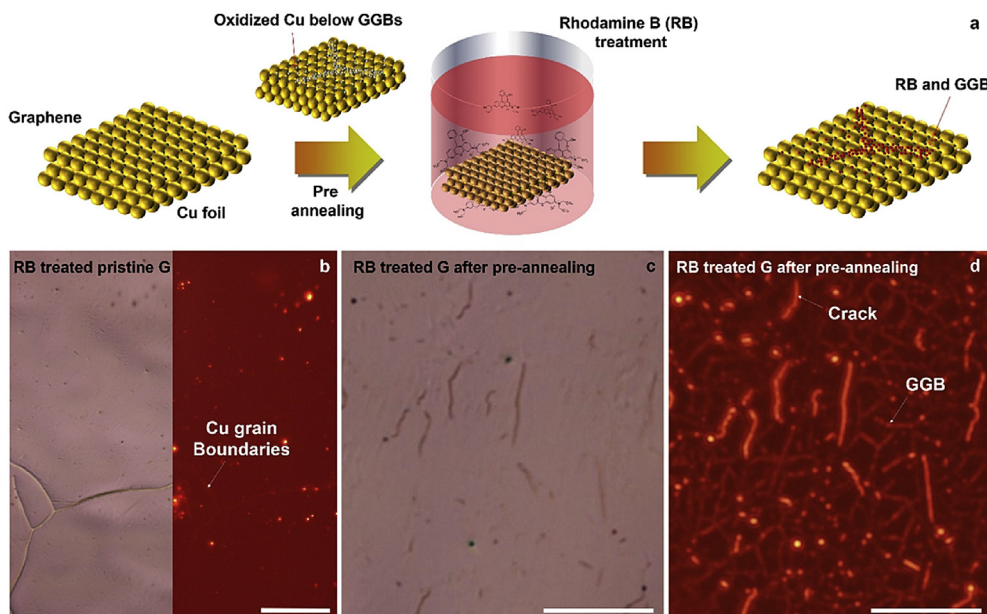
Fig. 1. Selective reaction of rhodamine B (RB) on graphene/Cu foil. (a) Pre-annealing and RB treatment of graphene/Cu foil. (b) Optical (left) and fluorescence (right) images of graphene treated with RB. (c) Optical and (d) fluorescence images of graphene treated with RB after pre-annealing. No difference in the optical image was evident before and after RB treatment. Graphene grain boundaries (GGBs; red lines) were observed in the fluorescence image. Scale bar in (b−d) is 10 μm. (A colour version of this figure can be viewed online.)
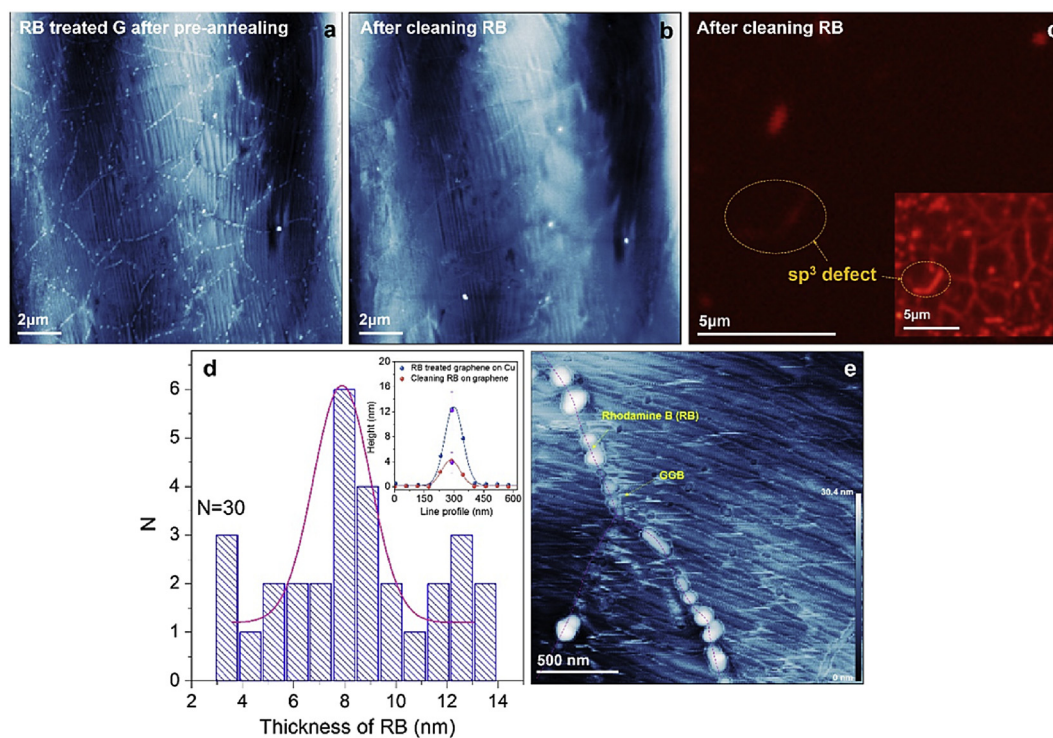
Fig. 2. RB surface morphology and thickness of RB molecules on RB treated graphene after pre-annealing. AFM image of RB-treated graphene (a) before and (b) after cleaning. (c) Fluorescence image of RB-treated graphene after removal of RB. The inset to (c) is a fluorescence image of RB-treated graphene. (d) Histogram of the thickness of RB molecules adsorbed on graphene from the AFM images in (a, b). The inset to (d) is the representative height before and after RB cleaning. The average thicknesses before and after RB cleaning are 12.17 ± 3.03 nm and 3.88 ± 1.65 nm, respectively. The thickness of RB molecules is 8.29 nm. (e) Morphology of RB molecules adsorbed on graphene. RB molecules exhibited a dot shape, and selective adsorption of RB on the graphene/Cu foil was observed. (A colour version of this figure can be viewed online.)

the fluorescence of RB on a hydrogenated graphene [22]. Pristine and hydrogenated graphene spin-coated with a dye layer (0.02% RB mixed with 5% PMMA in acetone) were characterized by fluorescence quenching microscopy, and dark areas (no fluorescence) and bright areas (red fluorescence) are pristine and hydrogenated graphene, respectively [22]. This was due to the weaker

fluorescence quenching ability of hydrogenated graphene due to their sp^3 hybridized carbon characteristic (loss of conjugation), compared to that of pristine graphene [22–25]. To validate the selective adsorption of RB molecules by sp^3 hybridized carbon in GGBs, we investigated the crystalline quality of graphene after pre-annealing and RB treatment using Raman spectroscopy and XPS. Generally, graphene defects can be estimated or quantified through the D-band in the Raman spectrum of graphene [26]. In each Raman spectrum in Fig. 3a, no enhancement of the D-band of graphene after pre-annealing and/or RB treatment was observed, resulting in few change in the I(D)/I(G) ratio, as shown in Fig. 3c. Pre-annealing in an oxygen environment and RB treatment processes do not affect the formation of additional defects on graphene, but tailor its electronic properties of graphene, Fig. 3b. The positions of the G and 2D band of graphene pre-annealed in an oxygen environment were blue-shifted compared to those of pristine graphene, from 1581 and 2689 cm^{-1} to 1601 and 2717 cm^{-1}, respectively, and the I(2D)/I(G) ratio was decreased due to adsorption of H_2O/O_2 molecules (hole doping) [27–29] or oxidized Cu. The positions of the G and 2D band of RB-treated graphene were red-shifted, similar to those of pristine graphene (Fig. 3b). This phenomenon may be related to adsorption of RB molecules on graphene.

The XPS spectra of C 1s of graphene were characterized before and after pre-annealing and RB treatment to accurately evaluate the variation in the sp^3 hybridized carbon concentration. The C 1s peaks consists of four components: sp^2 hybridized carbon (C=C) at 284.6 eV, sp^3 hybridized carbon (C–C) at 285.8 eV, C–O at 287.2 eV, and a carbonyl group (C=O) at 288.5 eV [30], and is observed in each C 1s XPS spectrum, as shown in Fig. 3d. After pre-annealing, the ratio of the sp^3 (C–C) and sp^2 (C=C) hybridized carbon

concentration was increased (0.26–0.33, brown circle in Fig. 3e) due to cracking of graphene (Supplementary Information Fig. S3 and Fig. 2c), and increases further after RB treatment due to C–C bonding with RB molecules (0.33–0.37, Fig. 3e). An increase in the concentration of sp^3 hybridized carbon and other functional groups in C 1s spectra were due to cracking of graphene and RB molecules. Their sp^3 hybridized carbon characteristics are not affected to the selective adsorption of RB molecules on GGBs because no additional defects on GGBs were formed by pre-annealing and RB treatment. The mechanism of the selective adsorption of RB molecules on GGBs after pre-annealing and RB treatment, therefore, should be addressed.

The graphene close to the GGB after pre-annealing can be strained by the hill structure of oxidized Cu or influenced by oxidized Cu (Fig. 4a), which may result in RB molecules being selectively adsorbed onto GGBs. The change in the electronic structure of strained graphene has been reported [31,32], and was directly related to the work function of graphene. We investigated the work function of graphene close to GGBs after pre-annealing using kelvin probe force microscopy (KPFM). The work function of Pt–Ir–coated Si tip was calibrated using highly oriented pyrolytic graphite (HOPG, Supplementary Information Fig. S4), and then the work function of graphene on the hill structure of oxidized Cu was measured (Fig. 4c and d). The surface potential of graphene on the hill of oxidized Cu was increased compared to that of pristine graphene on Cu, and its conversion to the work function yielded 0.025 ± 0.0043 eV. By AFM imaging (Figs. 2d and 4b), the uniaxial component of the strain at this structure was ~0.035%. Although the work function of graphene on the hill of oxidized Cu was increased, it is difficult to relate the increase in work function to the effect of strained graphene because the uniaxial strain of 0.035% of
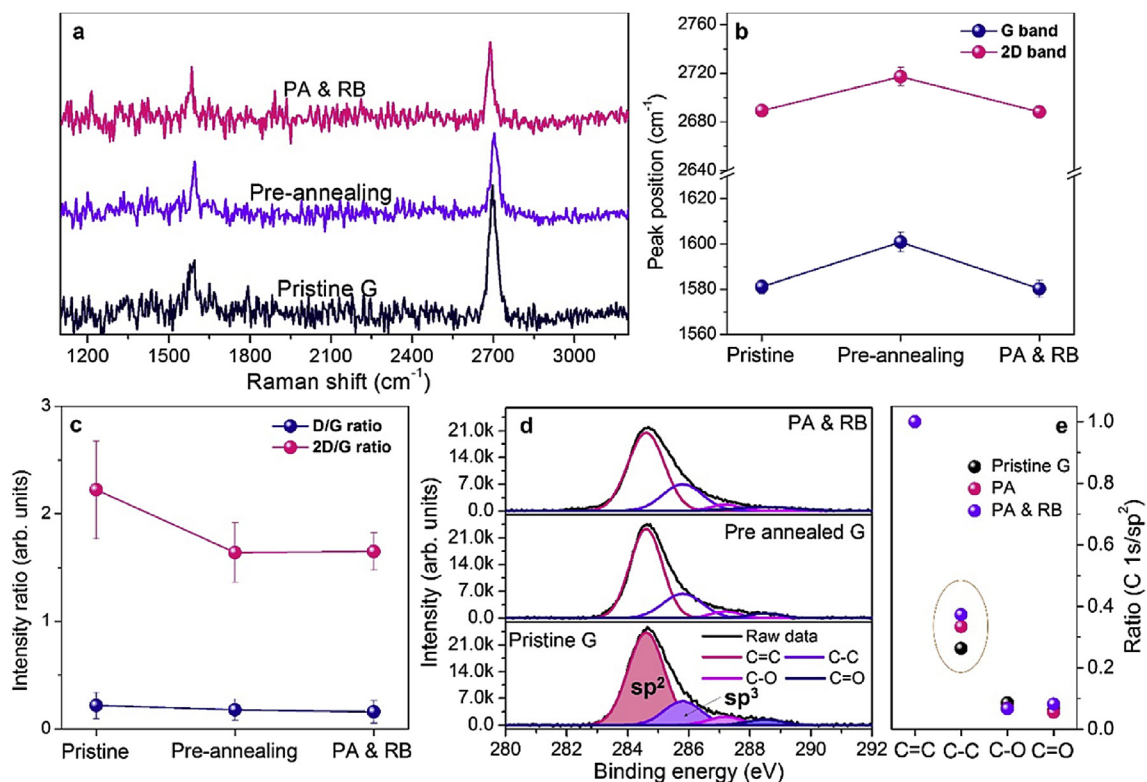
Fig. 3. Crystalline quality of RB treated graphene after pre-annealing. (a) Raman spectra, (b) G and 2D band positions, and (c) D/G and 2D/G ratios of pristine, pre-annealing (PA), and PA- and RB-treated graphene. No enhancement of the D-band of graphene after pre-annealing and RB treatment was observed. (d) XPS spectra of C 1s of graphene before and after pre-annealing and RB treatment, and (e) ratio of C 1s (four components: C=C, C–C, C–O, and C=O)/sp^2 hybridized carbon (C=C). (A colour version of this figure can be viewed online.)
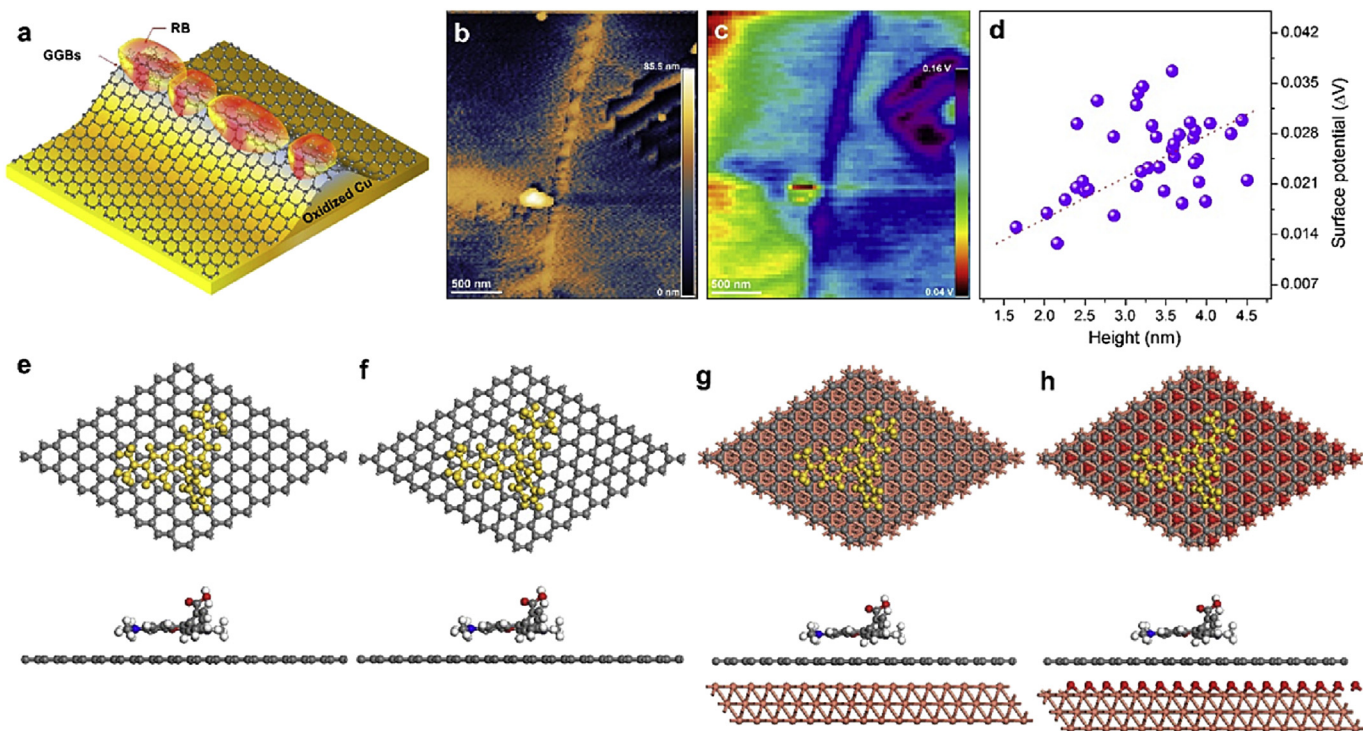
Fig. 4. Work function of graphene after pre-annealing, and binding energy of RB on four substrates. Scheme of (a) RB adsorbed on graphene at a hill structure of oxidized Cu beneath a GGB. (b) AFM and (c) KPFM images of graphene after pre-annealing, and (d) the altered surface potential of graphene on the hill of oxidized Cu was plotted against the height of the hill formed by pre-annealing. Top and side views of optimized RB structures on (e) pristine graphene, (f) strained graphene (0.035%), (g) graphene/Cu(111), and (h) graphene/O−Cu(111) surfaces. The binding energies of RB on (e−h) are 2.29, 2.42, 2.61, and 3.79 eV, respectively. The dark gray, white, blue and red balls represent carbon, hydrogen, nitrogen, and oxygen atoms, respectively. The RB molecule is shown in yellow in the top view to distinguish it from graphene. (A colour version of this figure can be viewed online.)
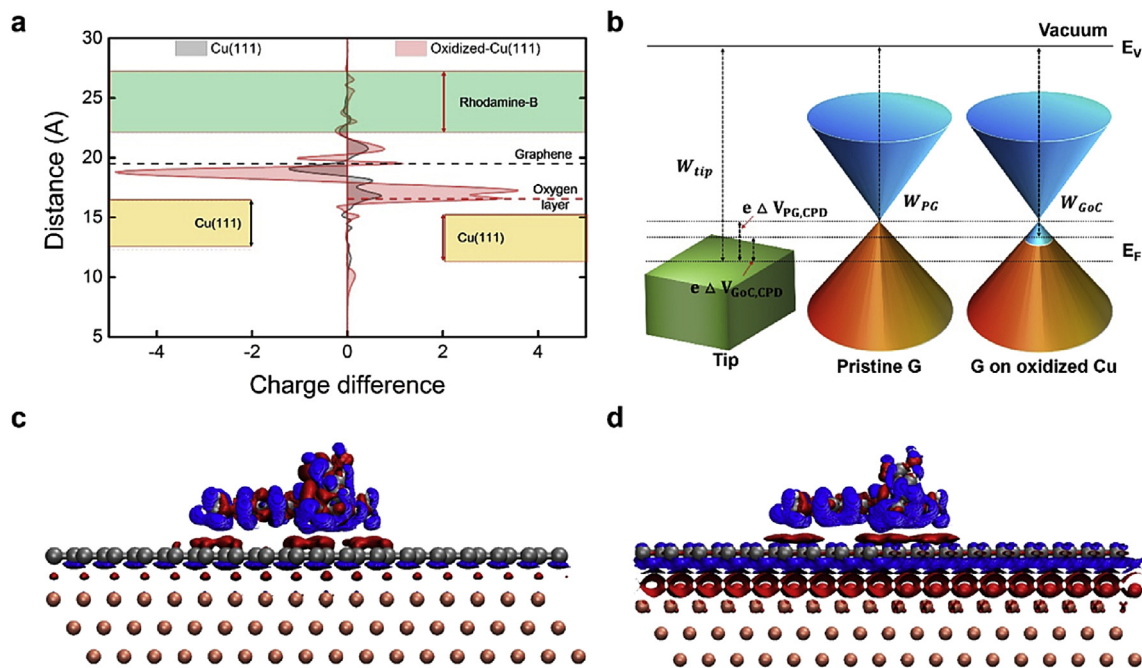
Fig. 5. Charge density between RB and graphene on Cu and oxidized Cu. (a) Charge density difference (CCD) of RB on graphene/Cu(111) and graphene/oxidized Cu(111) surface. (b) Scheme of the work function of pristine graphene on Cu and graphene on oxidized Cu obtained by KPFM. Charge density contour of RB on (c) graphene/Cu(111) and (d) graphene/oxidized Cu(111) surface. The red and blue balloons in (c) and (d) represent the charge accumulation and depletion, respectively. (A colour version of this figure can be viewed online.)

graphene rarely induced a change in work function or large shift of G-band position in the Raman spectrum of graphene [33,34]. The increased work function of graphene on the hill of oxidized Cu may

be related to increased p-doping concentration by oxidized Cu. We assume the increase in p-doping concentration with graphene on the hill of oxidized Cu to be caused by the interplay between

graphene and oxidized Cu. This is likely a key driving force for the selective adsorption of RB on GGB. Therefore, we investigated the binding energy between RB molecules and graphene on Cu or oxidized Cu to identify the cause of the change in work function and the key driving force of selective adsorption of RB molecules on GGB.

First, several initial structures of RB on graphene were considered by density function theory (DFT) calculation to identify the most stable configurations. The most stable structure of RB was located above the surface of graphene as oxygen atoms of carboxyl group (red ball) with RB are on the side distal from graphene (Fig. 4e). The binding energy of RB on various substrates, such as pristine graphene, strained graphene, graphene/Cu(111) and graphene/O–Cu(111), was calculated by DFT within the generalized gradient approximation (GGA) [15–18], as shown in Fig. 4e–h. The binding energy is defined as $E_b = -[E_{RB/sub} - E_{RB} - E_{sub}]$, where $E_{RB/sub}$, E_{RB}, and E_{sub} are the total energies of the combined system, RB, and substrate, respectively. The binding energies of RB on pristine and strained graphene are 2.29 and 2.42 eV, respectively. As mentioned above, because there is rarely a change in the electronic structure of graphene [20,33,34] and binding energy due to the hill structure (uniaxial strain of graphene, 0.035%), we consider RB placed on pristine graphene hereafter in this study. We investigated the binding strength between RB and graphene/Cu(111) or graphene/O–Cu(111) surface, where O–Cu(111) represents the oxidized Cu(111) surface, as shown in Fig. 4g and h. When RB was placed on the graphene/Cu(111) substrate, the binding energy (2.61 eV) was increased by ~0.32 eV per molecule, compared to pristine graphene. In RB on graphene/O–Cu(111), the binding energy (3.79 eV) was increased by ~1.18 eV, compared to graphene/Cu(111). Therefore, RB on the graphene/O–Cu(111) surface had the strongest binding energy among the four substrates considered, which is a key driving force of selective adsorption of RB molecules on GGB.

To investigate the charge distribution between RB and graphene/Cu(111) (or graphene/O–Cu(111)), we calculated the plane-averaged charge density in a perpendicular direction from the surface (Fig. 5). The charge density difference (CDD) in RB/graphene/Cu(111, black line) and RB/graphene/O–Cu(111, red line) system was obtained using the positions of RB, graphene, Cu(111), and O–Cu(111). To further illustrate the binding behaviors of RB on graphene/Cu(111) and graphene/O–Cu(111), we generated a contour plot of the CDD distribution in RB/graphene/Cu(111) and RB/graphene/O–Cu(111) (Fig. 5c and d). In the case of RB/graphene/Cu(111) system, electrons are accumulated above the Cu(111) surface and between RB and the graphene surface (black line, '+' CDD in Fig. 5a), while electrons are depleted beneath the graphene ('–' CDD in Fig. 5a). In the RB/graphene/O–Cu(111) system, electron accumulation and depletion are significantly increased between the O–Cu(111) surface and graphene, compared with that of Cu(111). Interestingly, electron accumulation and depletion occur simultaneously between RB and graphene, in contrast to Cu (111), and electron deficiency on the top and bottom side of graphene was observed (Fig. 5d). Positively charged graphene resulted from the electron deficiency in graphene by O–Cu(111), as an enhanced work function and p-doping behavior were observed by KPFM (Figs. 4c and 5b) and the projected density of state (PDOS) of graphene on O–Cu (Supplementary Information Fig. S5), respectively, which can trigger the polarization of RB, and, simultaneously, strongly adsorb polarized RB molecules on it due to Coulomb interactions.

4. Conclusion

In summary, we demonstrated the selective adsorption of RB molecules on GGBs by pre-annealing and immersion in RB. RB molecules on GGBs were clearly observed by FM, and important information on graphene, such as the grain size and crack distribution, was determined at a microscale. RB molecules on GGBs were easily removed by immersion in acetone. The work function of graphene on the hill structure of oxidized Cu was increased by oxidized Cu compared to that of pristine graphene. The strong binding energy of RB on graphene/O–Cu was calculated by DFT within the GGA. Since a pre-annealing process of Cu below GGBs yielded hill structures of oxidized Cu and, thereby, the p-doping behavior of graphene close to GGBs and selective adsorption of RB molecules on GGBs was mediated by the Coulomb effect between positively charged graphene and polarized RB molecules. This simple method of visualizing GGB will facilitate evaluation of the quality and reliability of other 2D materials.

Appendix A. Supplementary data

Supplementary data related to this article can be found at http://dx.doi.org/10.1016/j.carbon.2016.07.001.

References

[1] O.V. Yazyev, S.G. Louie, Electronic transport in polycrystalline graphene, Nat. Mater 9 (2010) 806–809.

[2] Q. Yu, L.A. Jauregui, W. Wu, R. Colby, J. Tian, Z. Su, et al., Control and characterization of individual grains and grain boundaries in graphene grown by chemical vapour deposition, Nat. Mater 10 (2011) 443–449.

[3] P.Y. Huang, C.S. Ruiz-Vargas, A.M. van der Zande, W.S. Whitney, M.P. Levendorf, J.W. Kevek, et al., Grains and grain boundaries in single-layer graphene atomic patchwork quilts, Nature 469 (2011) 389–392.

[4] K. Kim, Z. Lee, W. Regan, C. Kisielowski, M.F. Crommie, A. Zettl, Grain boundaries mapping in polycrystalline graphene, ACS Nano 5 (2011) 2142–2146.

[5] J. Tian, H. Cao, W. Wu, Q. Yu, Y.P. Chen, Direct imaging of graphene edges: atomic structure and electronic scattering, Nano Lett. 11 (2011) 3663–3668.

[6] H.I. Rasool, E.B. Song, M. Mecklenburg, B.C. Regan, K.L. Wang, B.H. Weiller, et al., Atomic-scale characterization of graphene grown on copper (100) single crystals, J. Am. Chem. Soc. 133 (2011) 12536–12543.

[7] H.I. Rasool, E.B. Song, M.J. Allen, J.K. Wassei, R.B. Kaner, K.L. Wang, et al., Continuity of graphene on polycrystalline copper, Nano Lett. 11 (2011) 251–256.

[8] L. Gao, J.R. Guest, N.P. Guisinger, Epitaxial graphene on Cu(111), Nano Lett. 10 (2010) 3512–3516.

[9] J.C. Koepke, J.D. Wook, D. Estrada, Z.-Y. Ong, K.T. He, E. Pop, et al., Atomic-scale evidence for potential barriers and strong carrier scattering at graphene grain boundaries: a scanning tunneling microscopy study,, ACS nano 7 (2013) 75–86.

[10] D.L. Duong, G.H. Han, S.M. Lee, F. Gunes, E.S. Kim, S.T. Kim, et al., Probing graphene grain boundaries with optical microscopy, Nature 490 (2012) 235–239.

[11] S. Lai, S.K. Jang, Y.J. Song, S. Lee, Probing graphene defects and estimating graphene quality with optical microscopy, Appl. Phys. Lett. 104 (2014) 043101.

[12] T.H. Ly, D.L. Duong, Q.H. Ta, F. Yao, Q.A. Vu, H.Y. Jeong, et al., Nondestructive characterization of graphene defects, Adv. Func. Mater 23 (2013) 5183–5189.

[13] D.W. Kim, Y.H. Kim, H.S. Jeong, H.T. Jung, Direct visualization of large-area graphene domains and boundaries by optical birefringency, Nat. Nanotechnol. 7 (2012) 29–34.

[14] J.-H. Son, S.-J. Baeck, M.-H. Park, J.-B. Lee, C.-W. Yang, J.-K. Song, et al., Detection of graphene domains and defects using liquid crystals, Nat. Comm. 5 (2014) 3484.

[15] G. Kresse, J. Furthmuller, Efficient iterative schemes for *ab initio* total-energy calculations using a plane-wave basis set, Phys. Rev. B 54 (1996) 11169.

[16] G. Kresse, J. Furthmuller, Efficiency of ab-initio total energy calculations for metals and semiconductors using a plane-wave basis set, Comput. Mater. Sci.

6 (1996) 15—50.

[17] J.P. Perdew, K. Burke, M. Ernzerhof, Generalized gradient approximation made simple, Phys. Rev. Lett. 77 (1996) 3865.

[18] S. Grimme, S. Antony, S. Ehrlich, S. Krieg, A consistent and accurate *ab initio* parametrization of density functional dispersion correction (DFT-D) for the 94 elements H-Pu, J. Chem. Phys. 132 (2010) 154104.

[19] L. He, Y.W. Liu, W.J. Tong, J.G. Lin, X.F. Wang, Surface energy engineering of Cu surface by strain: first-principles calculations, Surf. Rev. Lett. 20 (2013) 1350054.

[20] K.-A. Min, D. Sung, J. Ryou, G. Kim, S. Hong, Spatial variation in the electronic structures of carpetlike graphene nanoribbons and sheets, Curr. Appl. Phys. 14 (2014) 1687—1691.

[21] B.J. Fowler, B.D. Gelfand, Y. Kim, N. Kerur, V. Tarallo, Y. Hirano, et al., Nucle-oside reverse transcriptase inhibitors possess intrinsic anti-inflammatory activity, Science 346 (2014) 1000—1003.

[22] Z. Sun, C.L. Pint, D.C. Marcano, C. Zhang, J. Yao, G. Ruan, et al., Towards hybrid superlattices in graphene, Nat. Comm. 2 (2011) 559.

[23] J. Kim, L.J. Cote, F. Kim, J. Huang, Visualizing graphene based sheets by fluo-rescence quenching microscopy, J. Am. Chem. Soc. 132 (2010) 260—267.

[24] R. Lv, Q. Li, A.R. Botello-Mendez, T. Hayashi, B. Wang, A. Berkdemir, et al., Nitrogen-doped graphene: beyond single substitution and enhanced molec-ular sensing, Sci. Rep. 2 (2012) 586.

[25] X. Ling, L. Xie, Y. Fang, H. Xu, H. Zhang, J. Kong, et al., Can graphene be used as a substrate for Raman enhancement? Nano Lett. 10 (2010) 553—561.

[26] G. Xie, R. Yang, P. Chen, J. Zhang, Z. Tian, S. Wu, J. Zhao, M. Cheng, W. Yang, D. Wang, C. He, Z. Bai, D. Shi, G. Zhang, A general route towards defect and pore engineering in graphene, Small 10 (2014) 2280—2284.

[27] S. Ryu, S. Berciaud, Y.-J. Yu, H. Liu, P. Kim, G.W. Flynn, et al., Atmospheric oxygen binding and hole doping in deformed graphene on a SiO$_2$ substrate, Nano Lett. 10 (2010) 4944—4951.

[28] A. Das, S. Pisana, B. Chakraborty, S. Piscanec, S.K. Saha, U.V. Waghmare, et al., Monitoring dopants by Raman scattering in an electrochemically top-gated graphene transistor, Nat. Nanotechnol. 3 (2008) 210—215.

[29] D.-W. Shin, H.M. Lee, S.M. Yu, K.-S. Lim, J.H. Jung, M.-K. Kim, et al., A facile route to recover intrinsic graphene over large scale, ACS nano 6 (2012) 7781—7788.

[30] K.C. Kwon, K.S. Choi, S.Y. Kim, Increased work function in few-layer graphene sheets via metal chloride doping, Adv. Func. Mater 22 (2012) 4724—4731.

[31] N. Levy, S.A. Burke, K.L. Meaker, M. Panlasigui, A. Zettl, F. Guinea, et al., Strain-induced pseudo-magnetic field greater than 300 tesla in graphene nano-bubbles, Science 329 (2010) 544—547.

[32] W. Yan, W.-Y. He, A.-D. Chu, M. Liu, L. Meng, R.-F. Duo, et al., Strain and curvature induced evolution of electronic band structures in twisted graphene bilayer, Nat. Comm. 4 (2013) 2159.

[33] J.-U. Lee, D. Yoon, H. Cheong, Estimation of young's modulus of graphene by Raman spectroscopy, Nano Lett. 12 (2012) 4444—4448.

[34] S.-M. Choi, S.-H. Jhi, Y.-W. Son, Effects of strain on electronic properties of graphene, Phys. Rev. B 81 (2009) 081407.